

Bioinspired triboelectric droplet sensor for ammonia monitoring

Received: 7 March 2025

Accepted: 21 January 2026

Published online: 29 January 2026

 Check for updates

Tao Liu , Xuedi Li, Huanjie He, Kang Yu, Song Zhang , Ziyi Ye , Xue Cui, Bin Luo , Yanhua Liu, Mingchao Chi , Jinlong Wang , Chenchen Cai , Shuangfei Wang & Shuangxi Nie  

Gas sensors with fast response are in high demand for environmental and health applications. Conventional solid-state sensing materials are inherently constrained by response delays arising from chemical bond transformations, posing significant challenges in overcoming response time lag. In this work, inspired by the alveoli of our respiratory system, we develop a triboelectric nanogenerator probe sensor driven by the formation of water droplets containing an air cavity, which incorporates NH₃ molecules. The sensor achieves rapid response through instantaneous electron transfer at the liquid-solid interface, bypassing the need for gas adsorption and desorption on the surface of solid-state sensing materials. This hydro-electrochemical sensing mechanism achieves a response time of 1.4 s, surpassing that of most reported ammonia sensors. Through the integration of deep learning algorithms for optimization, the sensor demonstrates an ammonia detection accuracy of 96.2%. This study indicates a promising strategy for the rational design of gas sensors based on hydro-electrochemical sensing mechanisms.

Approximately 182 million tons of ammonia gas are produced globally each year, with about 80% ultimately being released into the atmosphere^{1,2}. The application of ammonia (NH₃) spans a wide range of sectors, including industry, agriculture, and healthcare³. Ammonia is a colorless gas with a pungent odor, and it is highly corrosive and toxic⁴. Prolonged exposure to ammonia concentrations greater than 50 ppm can lead to severe respiratory diseases and even death⁵. Efficient and accurate detection of ammonia is of paramount importance for both ecological environment and human health.

Ammonia's unique boiling point (−33.3 °C), refractive index (1.33), and dipole moment (1.42 D) make it a targeted gas of interest⁷. Based on the fundamental physical properties of ammonia, sensors utilizing resistance, optical, triboelectric, and microbalance principles have been developed, with resistive sensing being the mainstream commercial technology^{4–8}. Resistive sensors rely on the adsorption and desorption processes of ammonia on the surface of materials⁹. This dynamic transformation of chemical bonds inevitably introduces a reaction cycle, limiting the response speed of the

sensor¹⁰. Triboelectric nanogenerator probe (TENG-P) offers an in situ rapid detection solution, providing millisecond-level response capabilities through transient electron transfer at the liquid-solid interface^{11–13}. Nevertheless, conventional TENG-P lacks gas-sensing capabilities^{14,15}, and rationally designing gas sensors based on the hydroelectrochemical sensing mechanisms remains a challenge.

Alveoli are the core functional units of the biological respiratory sensing and regulatory system¹⁶. Through natural evolution and adaptation, alveoli have developed a spherical structure with internal cavities, endowing them with a highly efficient gas exchange interface and exceptional physiological stability (Fig. 1a-i). Oxygen diffuses from the alveoli into the bloodstream, binding with hemoglobin to form oxyhemoglobin, which is subsequently sensed by peripheral chemoreceptors to maintain blood oxygen concentrations within appropriate ranges (Fig. 1a-ii). Inspired by this natural design, an air-cavity droplet (A-droplet) driven ammonia gas sensor was developed in this work (Fig. 1b-i). Within the A-droplet, ammonia diffuses and dissolves in water, and its accompanying ionization generates a multitude of ions

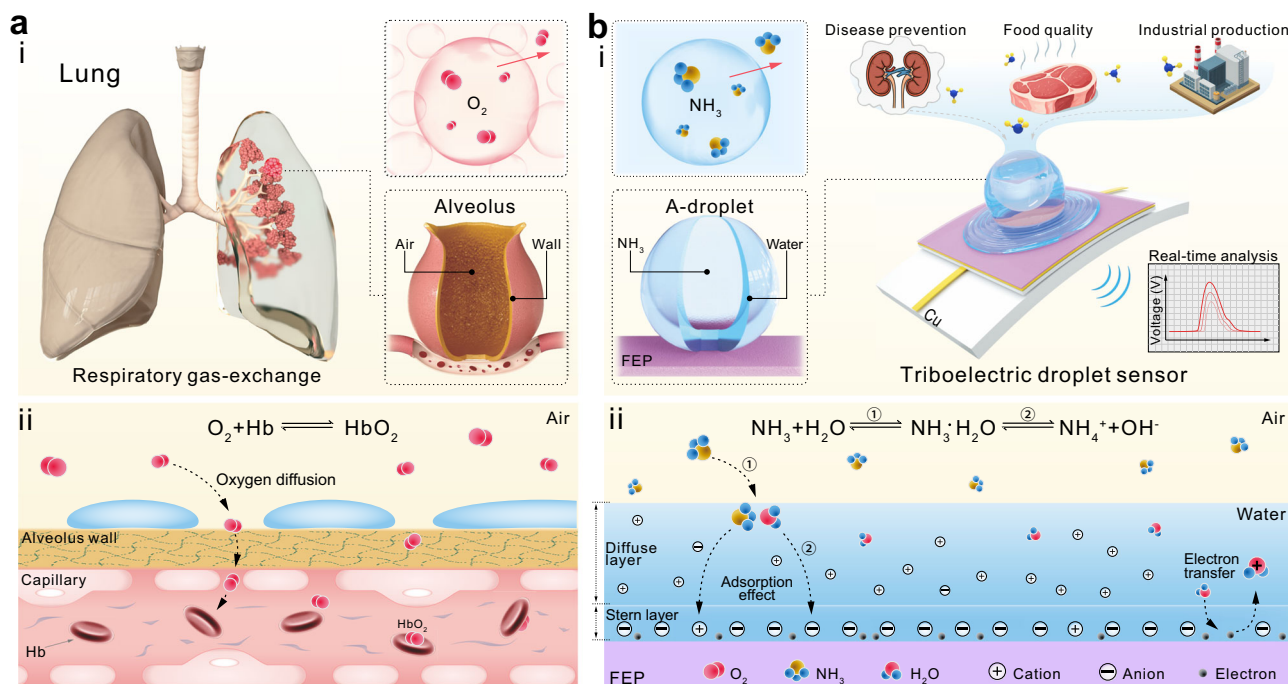


Fig. 1 | Bioinspired triboelectric droplet sensor. **a** Schematic diagram of alveolar structural characteristics and oxygen diffusion process, hemoglobin (Hb). **b** Schematic diagram of the structural features of the triboelectric droplet sensor

and ammonia diffusion process, illustration (ii) depicts the chemical reaction of ammonia dissolving in water and the influence of ammonium ions on charge transfer at the liquid-solid interface, fluorinated ethylene propylene (FEP).

that regulate the contact electrification process at the liquid-solid interface (Fig. 1b-ii). This operational principle enables the use of droplets as carriers for ammonia detection, offering the following potential performance advantages: (1) The gas response cycle of the sensor is shortened to 1.4 s, enhancing its potential for rapid ammonia detection; (2) the sensor's output stability is enhanced to 96.2%, contributing to improved sensing accuracy.

Results

Design of the droplet-driven ammonia sensor

The ammonia sensor is composed of an A-droplet preparation system and a TENG-P (Fig. 2a). The A-droplet is dispensed using a coaxial injection system, with droplet size controlled by the gas-liquid flow rate ratio (Fig. 2b, Supplementary Movie 1). Due to thin-film interference caused by bubbles within the A-droplet, the captured optical images exhibit irregular light and dark patterns. A gas-liquid flow rate ratio of 5:1 was selected due to its optimal TENG-P output stability (Supplementary Fig. 1). The TENG-P consists of a top electrode, a tribo-layer, a bottom electrode, and a connecting circuit. An insulated copper wire is used to connect the top electrode, ensuring its electrical isolation from the bottom electrode (Supplementary Fig. 2). When an A-droplet impacts the TENG-P, the sensor forms a closed-loop circuit and generates an output signal (Fig. 2c). Supplementary Movie 2 visually presents the real-time process of output generation driven by the A-droplet and demonstrates the sensor's continuous operation at a frequency of 2.5 Hz. The sensor exhibits an instantaneous output cycle of 2.1 ms, facilitating rapid target analyte detection (Supplementary Fig. 3).

When ammonia is loaded into the A-droplet, the sensor reaches a stable output after approximately four cycles (Fig. 2d). The sensing response time, defined as the interval from the onset of ammonia exposure to the attainment of a stable output, is determined to be 1.4 s (Fig. 2e). The response hysteresis of the sensor mainly arises from concentration gradient variations within the tube, caused by the thermal motion of ammonia molecules (Supplementary Fig. 4). The

sensor's response time is primarily governed by the droplet release frequency (Supplementary Fig. 5), rather than the ammonia concentration (Supplementary Fig. 6). The operating frequency exerts no significant influence on the sensor's output, indicating the feasibility of multiple working conditions (Supplementary Fig. 7). Moreover, direct blowing of ammonia does not elicit any sensor response, underscoring the necessity of introducing the A-droplet (Supplementary Fig. 8). These findings indicate that the sensor operates beyond the conventional response mechanisms of solid-state sensing materials, achieving a response speed that surpasses existing reports on ammonia sensors^{4–6,17–23}. Furthermore, the dual-fluid core-shell structure of the A-droplet exhibits impact resistance, effectively suppressing Kelvin-Helmholtz instability caused by droplet impact²⁴. The output stability of the TENG-P is enhanced to 96.2% by the A-droplet (Fig. 2f), surpassing that of most liquid-solid TENGs (Fig. 2g)^{25–34}.

Triboelectric response behavior

The output of the TENG-P is primarily governed by the liquid-solid contact area³⁵, as observed through high-speed camera imaging of the A-droplet impact and spreading process (Fig. 3a). Figure 3b illustrates the operational mechanism of the A-droplet-driven TENG-P. In the stationary state, the circuit of the TENG-P is open, and no electron flow occurs in the external circuit (State i). The impact of the A-droplet transitions the TENG-P to a "closed" state, inducing rapid electron flow towards the bottom electrode due to the potential difference between the top and bottom electrodes, generating the first current peak (Fig. 3c). Under the influence of gravitational potential and kinetic energy, the A-droplet gradually spreads outward, increasing the liquid-solid contact area, during which a slow rise in charge and voltage is detected (State ii). Upon reaching the maximum liquid surface spread, the potential between the electrodes equilibrates, ceasing electron flow (State iii). Subsequently, the droplet retracts and detaches from the top electrode, generating a reverse electron flow (State iv). Fluorinated ethylene propylene (FEP) was selected as the triboelectric

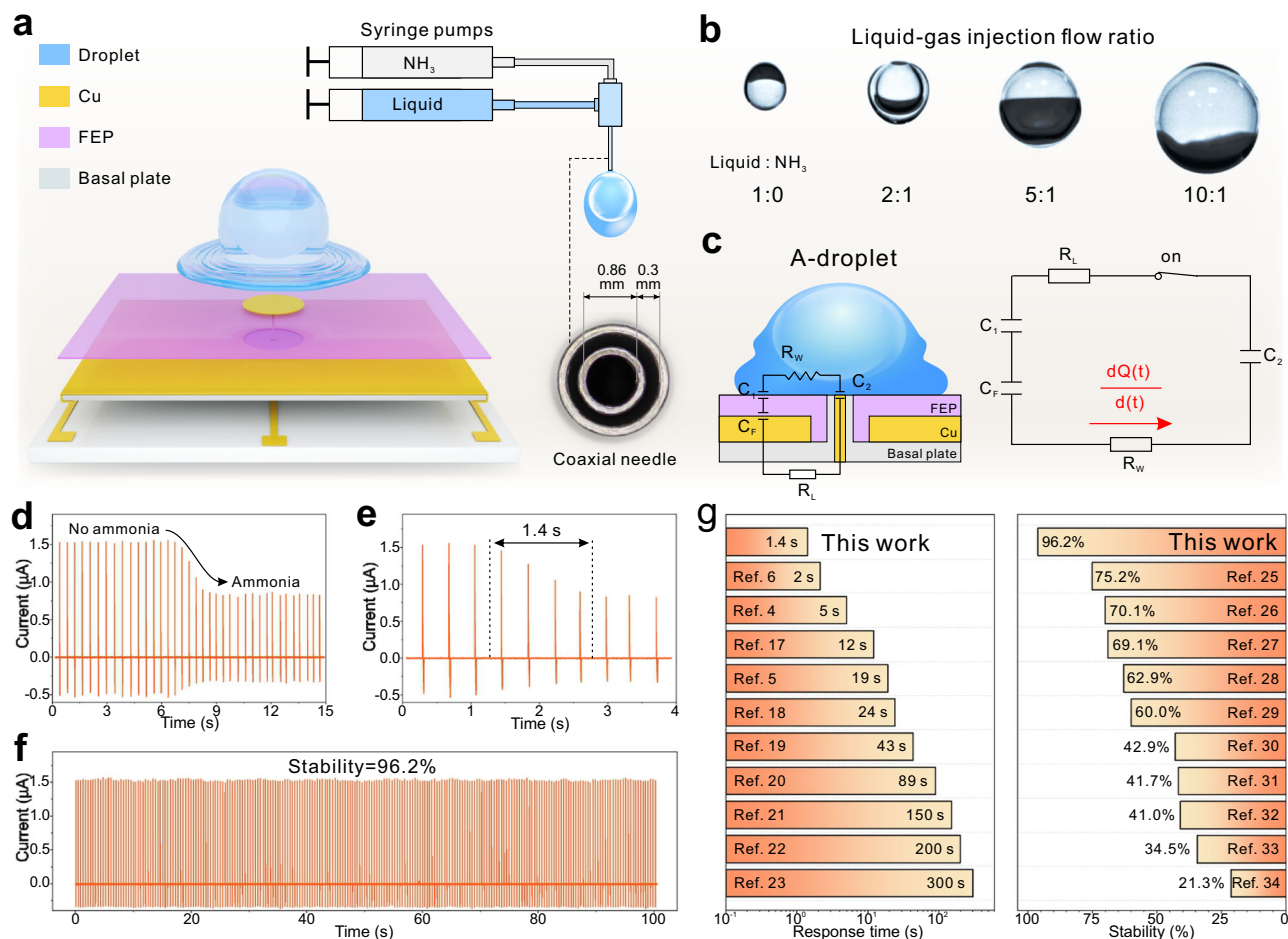


Fig. 2 | Ammonia sensor with fast response and stable output. **a** Schematic diagram of the sensor structure. **b** The effect of gas-liquid flow rate ratio on the shape and size of A-droplet. **c** Schematic diagram of the sensor's equivalent circuit.

d Cyclic response curve of the sensor to ammonia gas. **e** Response curve of sensor output. **f** Output curve of the sensor under long-term cycle. **g** Comparison of sensing performance of this work with other advanced reports.

layer material due to its superior sensing sensitivity, high resolution, and broad detection range (Supplementary Fig. 9). The material of the top electrode does not significantly affect the output (Supplementary Fig. 10). However, increasing its size inevitably limits the output, attributed to the finite liquid-solid contact area (Fig. 3d).

Characteristic images recorded by the high-speed camera show that the fluid morphology of the A-droplet is relatively smooth as it impacts and spreads to its maximum surface area (Fig. 3e). In contrast, conventional droplets exhibit numerous wrinkles and ripples (Supplementary Movie 3). The wrinkles formed by conventional droplets primarily originate during the initial spreading phase, rather than at the maximum spreading area (Supplementary Fig. 11). This phenomenon is attributed to Kelvin-Helmholtz instability generated by high-speed fluid motion²⁴, resulting in “noise” in the liquid surface spreading velocity (Fig. 3f, g). The irregular formation of wrinkles and ripples results in the difficulty of replicating the droplet's diffusion area (Supplementary Fig. 12), with conventional droplets displaying a maximum area deviation rate of 8.3% after repeated impacts (Fig. 3h). In contrast, the A-droplet's solid droplet exhibits an area deviation rate of only 1.9% (Fig. 3i). Consequently, the output fluctuations of the A-droplet-driven TENG-P are significantly lower than those of conventional droplets (Fig. 3j, k).

Optimization of sensing stability

Careful observation of the droplet impact phenomenon on solid surfaces provides further insight into the fluid characteristics of A-droplet. Both conventional droplets and A-droplets are released

from the same height and impact the solid surface, with selected snapshots of the impact-rebound evolution shown in Fig. 4a, b. In contrast to the rebound observed with conventional droplets, A-droplets exhibit oscillation after collision and rapidly remain on the surface (Supplementary Movie 4). Flow field distribution simulations reveal that during the contraction phase of conventional droplets, the fluid converges toward the center under the influence of surface tension and subsequently flows upward, resulting in a bounce (Supplementary Movie 5). In contrast, the A-droplet is influenced by the interplay of its inner and outer gas-liquid interfaces and simultaneously experiences both upward and downward surface tensions (Supplementary Fig. 13). Moreover, during the oscillation of the gas-liquid interface, the flow velocity alternates between upward and downward directions, thereby suppressing the rebound of the droplet (Supplementary Fig. 14).

When the release height of the droplet exceeds a critical threshold, the surface energy of the liquid is insufficient to counteract the impact kinetic energy, causing the droplet to break and form satellite droplets under slight perturbations (Fig. 4c). Observation of 100 droplet impact events revealed that the typical separation characteristic of conventional droplets is the formation of two satellite droplets (probability of 60.5%) (Supplementary Fig. 15). In contrast, A-droplet rarely produces satellite droplets, with a probability of only 8.8% for the formation of a single satellite droplet (Fig. 4d). The formation of satellite droplets detaches mass from the main droplet and reduces its kinetic energy. Therefore, kinetic energy (E_k) can be used to evaluate the instability during the droplet

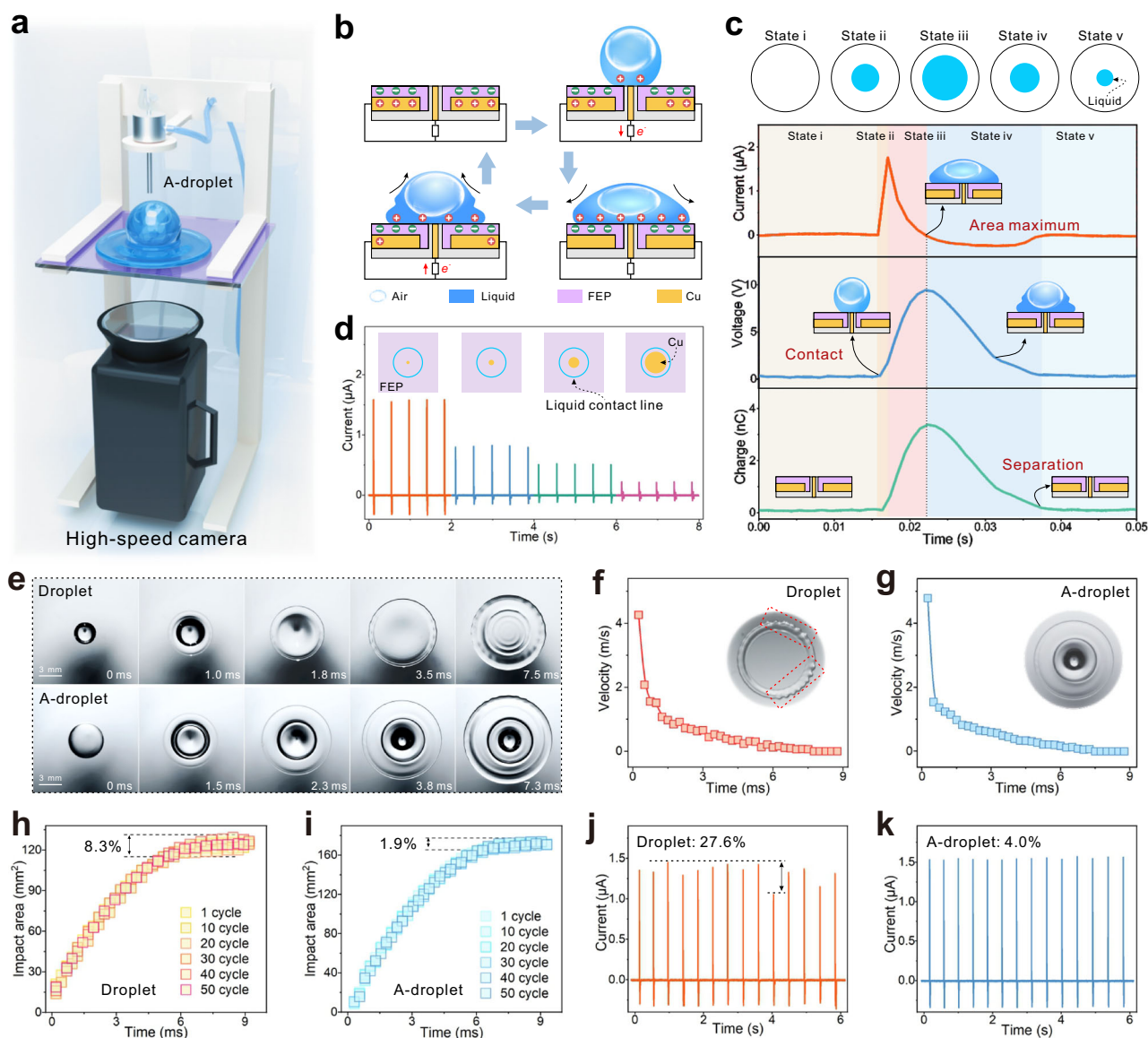


Fig. 3 | Working principle and performance of the sensor. **a** Schematic diagram of the fluid morphology of the A-droplet observed by the high-speed camera. **b** Working principle of the sensor. **c** Output curve corresponding to the fluid morphology. **d** Effect of electrode size on output, illustration shows the variation in electrode area, with the 4 different colored lines corresponding to the different

electrode areas they are beneath. **e** Characteristic images of droplet and A-droplet impact diffusion. **f, g** Curves of droplet and A-droplet diffusion velocities, with insets showing the corresponding fluid morphology. **h, i** Deviation rates of droplet and A-droplet driven TENG-P. **j, k** Signal deviation rates of droplet and A-droplet driven TENG-P.

rebound process. Detailed calculations are provided in Section S1 (Supplementary Fig. 16). Compared to conventional droplets, the rebound kinetic energy of A-droplet is reduced by 72.3% (Supplementary Fig. 17), indicating that most of the rebound kinetic energy is dissipated by the air cushion, thereby suppressing droplet rebound and fragmentation (Supplementary Movie 6).

The impact kinetic energy of the A-droplet can be modulated by adjusting the release height, with output intensity exhibiting a positive correlation with release height (Fig. 4e). When the release height is increased to 10 cm, output fluctuation increases to 9.8% (Fig. 4f). This is attributed to excessive droplet stretching (Supplementary Fig. 18), leading to unstable droplet spreading. An optimal output and stability are achieved at an impact angle of 45° (Fig. 4g, h). This is due to the balance between tangential and normal forces experienced by the droplet after impact at a 45° angle (Supplementary Fig. 19), resulting in optimal fluid spreading area post-impact.

Response mechanisms for ammonia monitoring

Building on the stability optimization of the A-droplet and an understanding of its underlying principles, it is crucial to further elucidate the mechanism of its response to ammonia. A-droplet exhibits stable existence at room temperature without noticeable volume shrinkage (Fig. 5a), negating the influence of droplet morphology on the ammonia response mechanism. After ammonia absorption by the solution, the water contact angle on the dielectric surface exhibits no significant deviation (Supplementary Fig. 20), thereby excluding the influence of wettability on liquid–solid contact electrification. Molecular simulations reveal that the interaction energies of H₂O–H₂O, NH₃–H₂O and NH₃–NH₃ are $-4.53 \text{ kcal mol}^{-1}$, $-7.06 \text{ kcal mol}^{-1}$ and $-3.41 \text{ kcal mol}^{-1}$, respectively (Fig. 5b), indicating that ammonia gas is more inclined to combine with water. FTIR analysis reveals that the dissolution of ammonia causes a shift in the O–H peak, confirming that the dissolved ammonia molecules disturb the hydrogen bonding

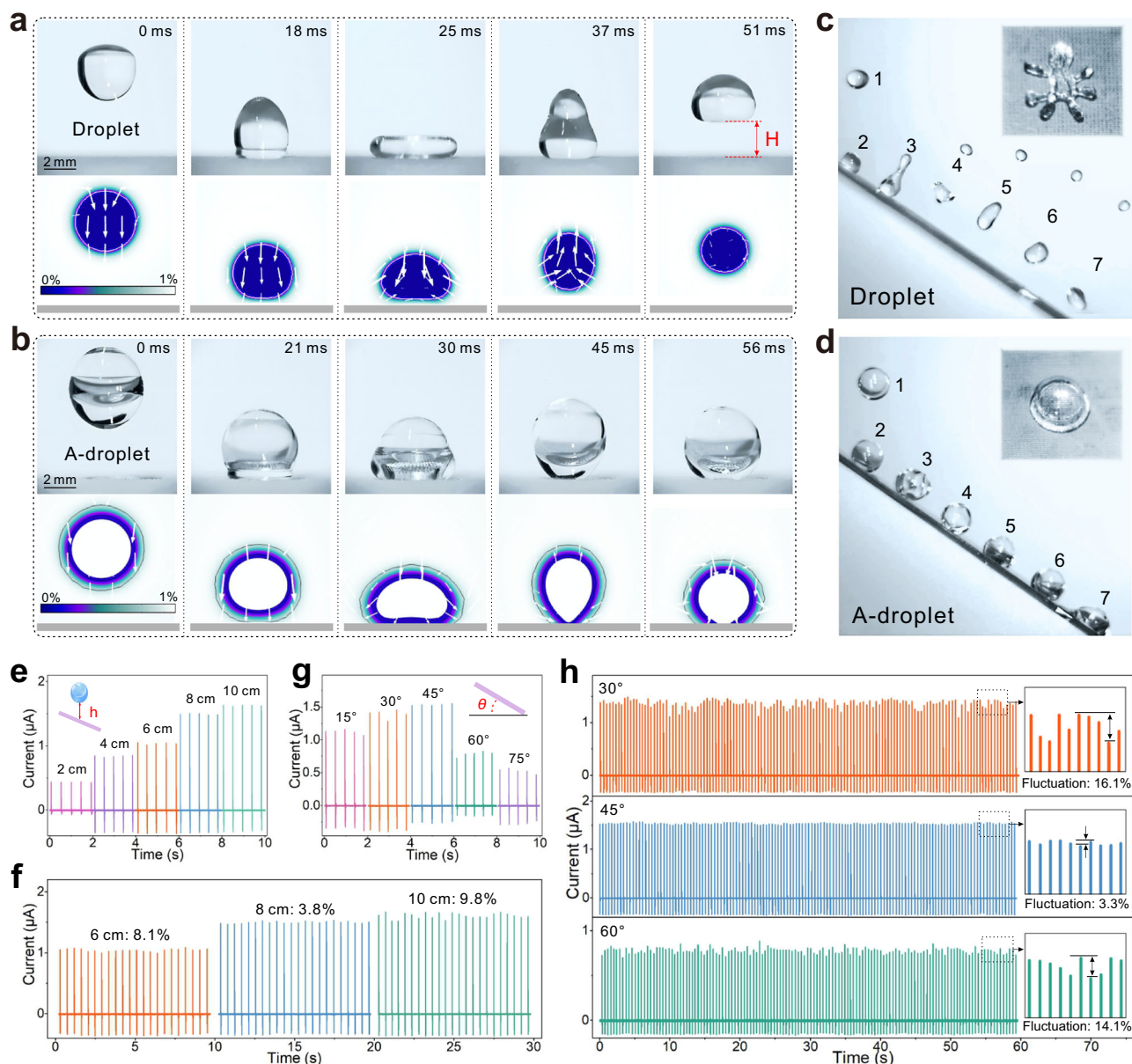


Fig. 4 | Hydrodynamic behavior and output stability of A-droplet.

a Characteristic images and fluid simulation of conventional droplet impact rebound. **b** Characteristic images and fluid simulation of A-droplet impact rebound. **c** Characteristic image of conventional droplet impact fragmentation, this is a

combination of images taken at different times. **d** Characteristic image of sliding after A-droplet impacts, this is a combination of images taken at different times. **e, f** Effects of A-droplet release height on output and stability. **g, h** Effects of TENG-P tilt angle on output and stability.

network of the water molecules (Fig. 5c)^{36–38}. Such significant intermolecular interactions are not observed in other gases, such as H_2S , CH_4 , O_2 , N_2 , and CO (Supplementary Fig. 21), rendering them poorly absorbed by water. The sensor's response to these common gases is negligible (Fig. 5d). Even when these gases are mixed with ammonia, no significant signal deviation is observed (Supplementary Fig. 22), underscoring ammonia as the critical marker for the sensor's selective recognition.

The sensor is capable of detecting ammonia concentration variations within the 0–200 ppm range, with its sensitivity defined by the slope of the output change, $[(I_0 - I) / I_0]$ (Fig. 5e), where I_0 and I represent the currents in the absence and presence of ammonia, respectively. The sensor exhibits an excellent linear response, indicating high accuracy in its measurements. Moreover, the sensor output remains relatively stable across different ammonia concentrations

(Fig. 5f), demonstrating reliable operation under a constant ammonia atmosphere. By optimizing the gas injection setup, the sensor can be directly interfaced with the ambient environment, highlighting its potential for applications in open-air ammonia detection (Supplementary Fig. 23). Continuous monitoring over 192 h was conducted to investigate the influence of varying temperature and humidity in open environments on the sensor performance (Supplementary Fig. 24). The sensor shows an output deviation of less than 10% within the 0–50 °C range and less than 15% under 50–90% RH (Supplementary Figs. 25 and 26), with signal variations likely arising from changes in ammonia solubility and humidity-induced suppression of contact electrification. Notably, these environmentally induced signal deviations can be further corrected through algorithmic calibration⁵.

Upon dissolution in water, ammonia (NH_3) readily accepts a proton from H_2O , forming ammonium ions (NH_4^+) and generating

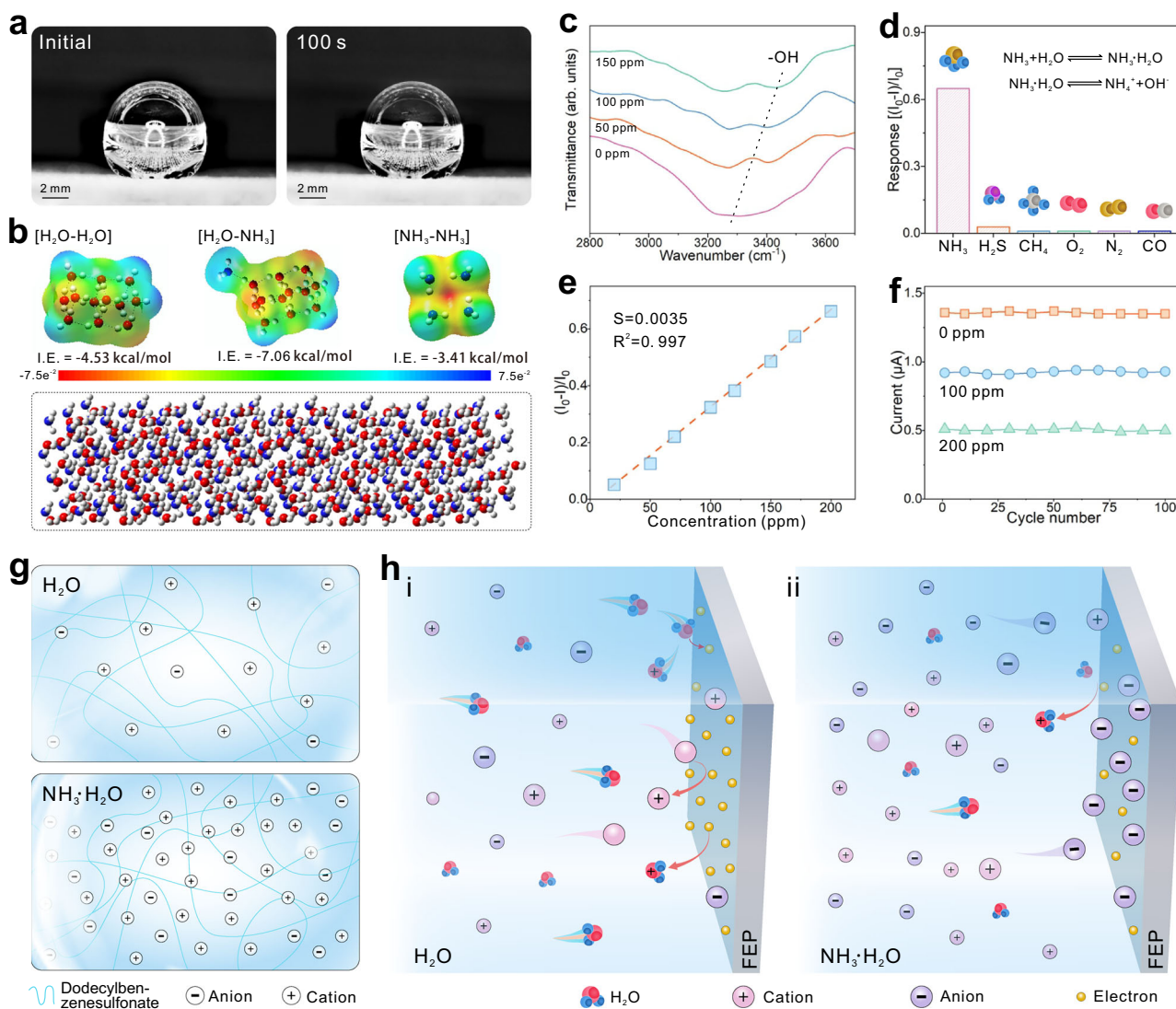


Fig. 5 | Principle of contact initiation at the liquid-solid interface. **a** A-droplet's feature image. **b** Molecular simulations of NH_3 and H_2O . **c** FTIR of ammonia dissolved in water. **d** Sensor responsiveness to different gases. **e** Sensitivity of

ammonia sensor. **f** Output Stability of ammonia sensor. **g** Schematic representation of ion concentrations in aqueous and ammonia solutions. **h** Schematic diagram of the liquid-solid contact electrification for water and ammonia solutions.

hydroxide ions (OH^-)³⁹. The spontaneous ionization of aqueous ammonia leads to an increase in solution conductivity and pH (Supplementary Fig. 27). Compared to the initial solution, the A-droplet infused with ammonia carries a substantial ionic load (Fig. 5g). Electron transfer and ion adsorption proceed in parallel during the contact electrification process at the liquid-solid interface⁴⁰. For aqueous solutions with low ion concentrations, electron transfer predominates⁴¹. When droplets impact the dielectric surface, fluorine-containing functional groups with strong electron retention capabilities acquire electrons from water molecules or even ions (Fig. 5h-i). Conversely, for A-droplet containing dissolved ammonia and abundant ions, competitive ion adsorption occupies a significant number of electron transfer sites, limiting the ability of fluorine-containing functional groups to extract electrons from water (Fig. 5h-ii). Further increases in solution ion concentration result in an excess of free ions, leading to a more pronounced shielding effect. As the A-droplet departs from the FEP surface, it carries away a substantial quantity of ions, resulting in negligible residual nitrogen on the FEP surface (Supplementary Fig. 28). The structural and elemental stability of the FEP surface indirectly corroborates the sensor's output consistency.

This ion-mediated contact electrification process at the liquid-solid interface provides an effective pathway for utilizing A-droplet to respond to ammonia concentrations.

Real-time ammonia concentration response

Approximately 90% of global ammonia emissions originate from agriculture, primarily from fertilizers and animal manure². In typical greenhouse environments⁴², efficient and accurate ammonia monitoring is crucial for both plant growth and human health (Supplementary Fig. 29). The integration of ammonia sensors in agricultural production, coupled with wireless sensing and artificial intelligence technologies, enables interdisciplinary intelligent data analysis and facilitates more precise environmental monitoring in agriculture (Fig. 6a). A coaxial injector, a triboelectric droplet sensor, and a wireless sensing module are integrated into a single ammonia sensing platform, with the sensor directly connected to the wireless module (Fig. 6b). When the A-droplet is generated by the top coaxial injector and released downward, the electrical signal produced by the triboelectric droplet sensor enters a signal modulation circuit composed of transistors and resistors. The circuit adjusts the signal amplitude

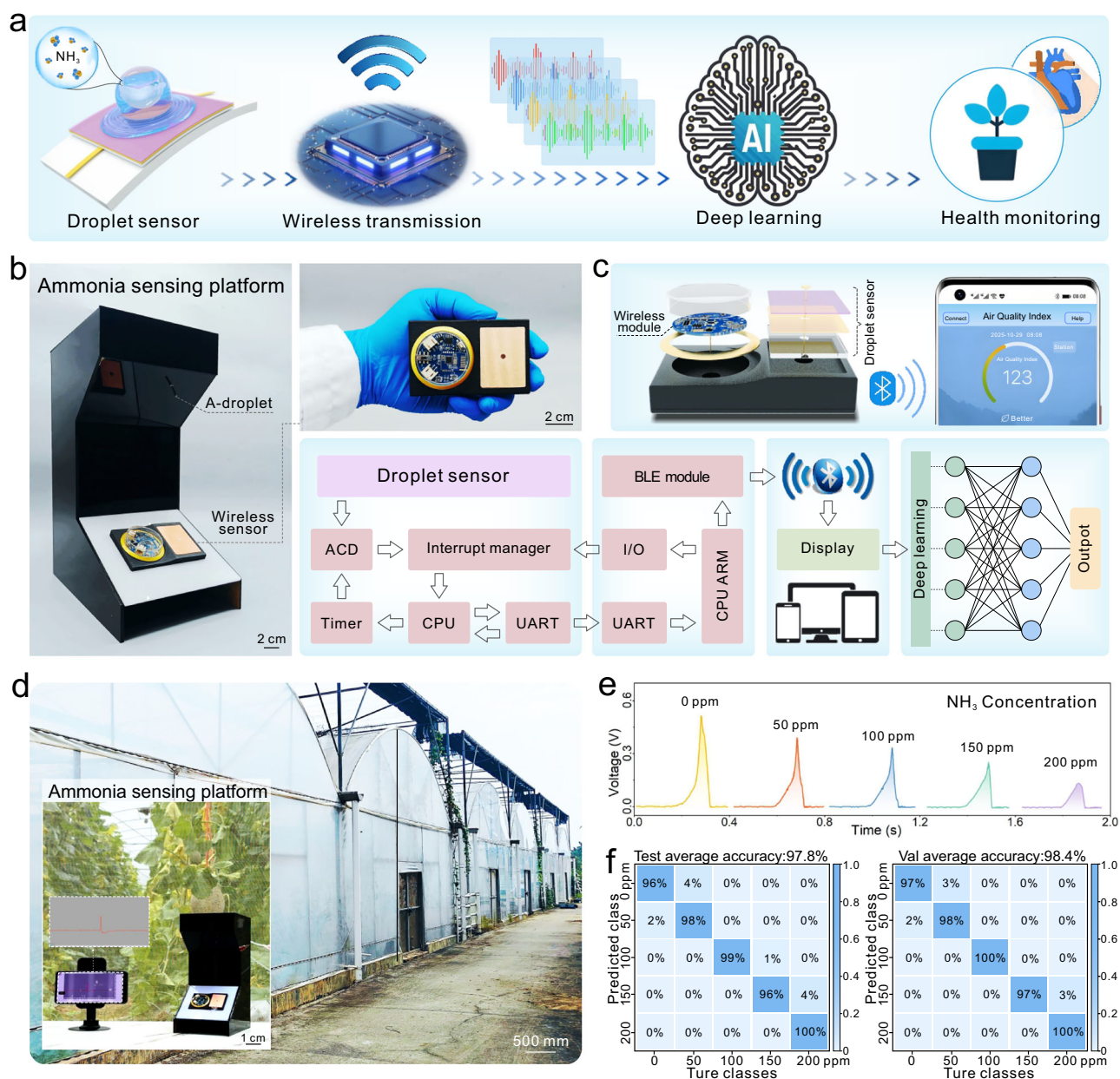


Fig. 6 | Design and application demonstration of the ammonia sensing platform. **a** Technical framework of the ammonia sensing platform. **b** Photograph of the ammonia sensing platform, with an inset illustrating the schematic of the wireless sensor and electronic architecture. **c** Schematic of the wireless connection

between the sensor and the intelligent display device. **d** Demonstration photograph of the platform in application. **e** Wireless response curves. **f** Confusion matrix for ammonia concentration identification results.

before it is transmitted to the analog-to-digital converter (ADC) of a microcontroller, converting multi-channel analog signals into digital form for processing by the central processing unit. Finally, the Bluetooth module transmits the processed digital signals in real time to intelligent display devices at high transmission rates (Fig. 6c).

Based on the triboelectric sensor's capability to respond in open environments (Supplementary Fig. 23), the ammonia sensing platform can be applied to environmental monitoring in greenhouses (Fig. 6d). Supplementary Movie 7 visualizes the wireless sensing capability of the platform, with the intelligent display device providing real-time responses without latency. When ammonia contamination occurs in the ambient environment, the platform generates a pronounced concentration response (Fig. 6e). The transmitted data signals to the intelligent display device can be further analyzed using a convolutional

neural network (CNN) architecture to enhance ammonia concentration recognition⁴³. This model employs a hierarchical feature-extraction framework, comprising an input layer, multi-level convolutional and pooling modules, fully connected layers, and a Softmax classifier, enabling stepwise extraction of time-frequency image features for ammonia concentration classification (Supplementary Fig. 30). With increasing training iterations, the model demonstrates high training accuracy (Supplementary Fig. 31), indicating stable convergence during training. Following extensive training, testing, and validation, the model's recognition accuracy for ammonia concentrations improved from 97.8% to 98.4% (Fig. 6f). These results demonstrate that the ammonia sensing platform can accurately detect ammonia and holds potential for developing multifunctional gas-sensing platforms.

Discussion

This study has demonstrated the efficacy of employing A-droplet for gas sensing and has developed an ammonia concentration sensor based on liquid-solid contact electrification. The sensor exhibits exceptional response time and stability, offering a valuable reference for constructing versatile gas-sensing platforms. In the future, rational design of the coaxial injection system is expected to significantly enhance the platform's ammonia responsiveness and adaptability in open environments. The successful integration of deep learning techniques effectively enhances the accuracy of ammonia concentration recognition. Furthermore, the inherent anti-rebound and anti-fragmentation properties of A-droplet enhance impact resistance, potentially generating intriguing new phenomena and functionalities in the field of droplet dynamics. By judiciously tailoring the internal structural composition of A-droplet, a plethora of counterintuitive phenomena and valuable applications can be envisioned.

Methods

Preparation of A-droplet

Two syringe pumps (LINA-8A, LAIN) were employed to drive a co-flow microfluidic device for producing A-droplets, with air and liquid serving as the inner and outer phase fluids, respectively. A 0.1 wt% solution of sodium dodecylbenzenesulfonate (Macklin, 95%) was used as the liquid phase, while ambient air represented the gas phase. The inner diameter of the coaxial needle was 0.86 mm, and the inner diameter of the outer capillary was 1.55 mm. To sustain continuous A-droplet production, the flow rate of the outer liquid phase was maintained between 20 mL·h⁻¹ and 200 mL·h⁻¹, with the inner gas flow rate controlled at 20 mL·h⁻¹. Ordinary droplets can be considered as A-droplets with zero gas content and were generated using the same solution. Ammonia gas was generated via heated evaporation of aqueous ammonia and subsequently stored in sample bags. Different concentrations of ammonia were prepared by mixing ammonia gas with air at predetermined ratios, with concentrations verified using an ammonia detector (JXBS-4001, BAIBOLI). The ammonia gas was then introduced as the gas source into a co-flow microfluidic device for the generation of A-droplets.

Fabrication of TENG-P

A laser cutter was used to etch circular holes with approximately 1 mm diameter in an acrylic plate (1 mm thickness), serving as the supporting substrate. Copper tape (100 μm thickness) and FEP tape (80 μm thickness) were sequentially adhered onto the acrylic plate, functioning as the bottom electrode and tribo-layer, respectively. Subsequently, an insulated copper wire (0.3 mm diameter) with an insulating layer was inserted through the circular hole of the acrylic plate, penetrating the bottom electrode and tribo-layer. The protruding copper wire was affixed to the upper surface of the tribo-layer with a copper sheet (~3 mm diameter), forming the top electrode. A copper wire (0.3 mm diameter) was led out from the bottom electrode, yielding a TENG-P with a dual-electrode structure (Supplementary Fig. 2).

Observation of droplet morphology

A high-speed camera (FASTCAM Mini AX200, Photron) was used to record the impact process at frame rates ranging from 1000 FPS to 5000 FPS. For the observation of the droplet's bottom morphology, the high-speed camera was positioned vertically, with a horizontal transparent acrylic plate (2 mm thickness) placed above the camera. Droplets were released from a height of 10 cm above the acrylic plate.

Characterization and testing

A metallurgical microscope (TD-D-4KE, SANQITID) was used to document the generation process of A-droplets at 60 FPS. The output of the TENG-P was recorded using an electrometer (6514, KEITHLEY),

acquiring the short-circuit current generated by A-droplet and conventional droplet impacts. Unless otherwise specified, the operating frequency of the A-droplet is maintained at 2.5 Hz. Fourier transform infrared spectroscopy (SENSOR II, BRUKER) was used to analyze changes in chemical functional groups. Surface morphology and elemental composition of the materials were characterized using a scanning electron microscope coupled with energy-dispersive X-ray spectroscopy (GeminiSEM 300, ZEISS). Water contact angles were measured employing a contact angle goniometer (DSA100, KRUSS).

Deep learning

Signal classification was implemented using the YOLO11 algorithm within the Ultralytics framework, employing a CNN architecture to analyze the time–frequency images derived from triboelectric signals. The model architecture comprises an initial convolutional layer for feature extraction across three stages, with C3k2 and C2PSA modules enabling multi-scale feature fusion, and a final Classify layer outputting five ammonia concentration levels. The dataset consists of 6000 images, partitioned into training, validation, and test sets in a 6:3:1 ratio. The YOLO11 classification model was configured for transfer learning based on the pre-trained YOLO11x-cls weights, successfully transferring 234 out of 236 weight parameters. Training was conducted on an NVIDIA RTX 4070 GPU for 100 epochs, employing an adaptive learning rate schedule to optimize convergence, with eight data-loading threads for parallel processing and a batch size of 16. The output layer utilizes a Softmax activation function to classify five ammonia concentration levels (0, 50, 100, 150, 200 ppm), and classification accuracy was optimized using the cross-entropy loss function.

Numerical simulation

Flow distribution was calculated using ANSYS Fluent software, and the Volume of Fluid method was employed to simulate the dynamic processes on the surface of A-droplet and conventional droplets. The droplet was simulated within a cylindrical domain with a width of 12 mm and a height of 10 mm. A superhydrophobic contact angle was applied to the bottom region, and the surface of the other regions was set as a pressure outlet boundary. The Pressure-Velocity Coupling method was used to solve the pressure and velocity coupling equations. For the two phases, the primary phase was set as air, and the secondary phase was set as liquid. In the initial stage, the water droplet was simulated as a sphere with a downward impact velocity.

Reporting summary

Further information on research design is available in the Nature Portfolio Reporting Summary linked to this article.

Data availability

The data that supports the findings of the study are included in the main text and supplementary information files. Source data are provided with this paper.

References

1. Fu, X. et al. Continuous-flow electrosynthesis of ammonia by nitrogen reduction and hydrogen oxidation. *Science* **379**, 707–712 (2023).
2. Behera, S. N., Sharma, M., Aneja, V. P. & Balasubramanian, R. Ammonia in the atmosphere: a review on emission sources, atmospheric chemistry and deposition on terrestrial bodies. *Environ. Sci. Pollut. R.* **20**, 8092–8131 (2013).
3. Aarya, S., Kumar, Y. & Chahota, R. K. Recent advances in materials, parameters, performance and technology in ammonia sensors: a review. *J. Inorg. Organomet. P.* **30**, 269–290 (2020).
4. Wang, S. et al. Fabrication of robust and cost-efficient Hoffmann-type MOF sensors for room temperature ammonia detection. *Nat. Commun.* **14**, 7261 (2023).

5. Lv, W. et al. Wide-range and high-accuracy wireless sensor with self-humidity compensation for real-time ammonia monitoring. *Nat. Commun.* **15**, 6936 (2024).
6. Zhao, J. et al. Multiscale structural triboelectric aerogels enabled by self-assembly driven supramolecular winding. *Adv. Funct. Mater.* **34**, 2400476 (2024).
7. Mazur, F., Han, Z., Tjandra, A. D. & Chandrawati, R. Digitalization of colorimetric sensor technologies for food safety. *Adv. Funct. Mater.* **36**, 2404274 (2024).
8. Zhang, S. et al. Smart lanceolate surface with fast fog-digesting performance for triboelectric energy harvesting. *ACS Nano* **18**, 21316–21325 (2024).
9. Timmer, B., Olthuis, W. & Berg, A. v. d. Ammonia sensors and their applications—a review. *Sens. Actuators B Chem.* **107**, 666–677 (2005).
10. Kwak, D., Lei, Y. & Maric, R. Ammonia gas sensors: a comprehensive review. *Talanta* **204**, 713–730 (2019).
11. Zhang, J., Lin, S. & Wang, Z. L. Triboelectric nanogenerator array as a probe for in situ dynamic mapping of interface charge transfer at a liquid-solid contacting. *ACS Nano* **17**, 1646–1652 (2023).
12. Xu, W., Li, X., Brugger, J. & Liu, X. Study of the enhanced electricity output of a sliding droplet-based triboelectric nanogenerator for droplet sensor design. *Nano Energy* **98**, 107166 (2022).
13. Ye, Z. et al. Bioinspired superhydrophobic triboelectric materials for energy harvesting. *Adv. Funct. Mater.* **35**, 2412545 (2025).
14. Liu, T. et al. Liquid-solid triboelectric probes for real-time monitoring of sucrose fluid status. *Adv. Funct. Mater.* **33**, 2304321 (2023).
15. Luo, B. et al. Triboelectric charge-separable probes for quantitatively charge investigating at the liquid-solid interface. *Nano Energy* **113**, 108532 (2023).
16. Mendenhall, R. M. & Sun, C. N. Surface lining of lung alveoli as a structure. *Nature* **201**, 713–714 (1964).
17. Zhang, W. et al. Gas-sensitive cellulosic triboelectric materials for self-powered ammonia sensing. *Adv. Sci.* **9**, 2203428 (2022).
18. Gao, C. et al. Hierarchical porous triboelectric aerogels enabled by heterointerface engineering. *Nano Energy* **121**, 109223 (2024).
19. Zhang, S. et al. Field effect transistor sensors based on in-plane 1T '2H/1T' MoTe₂ heterophases with superior sensitivity and output signals. *Adv. Funct. Mater.* **32**, 2205299 (2022).
20. Wang, S. et al. Ultrasensitive flexible self-powered ammonia sensor based on triboelectric nanogenerator at room temperature. *Nano Energy* **51**, 231–240 (2018).
21. Wang, Q. et al. High-performance room temperature ammonia sensors based on pure organic molecules featuring B-N covalent bond. *Adv. Sci.* **11**, 2308483 (2024).
22. Guo, S. et al. Development of a cloud-based epidermal MoSe₂ device for hazardous gas sensing. *Adv. Funct. Mater.* **29**, 1900138 (2019).
23. Chen, H. et al. Suspended SnS₂ layers by light assistance for ultrasensitive ammonia detection at room temperature. *Adv. Funct. Mater.* **28**, 1801035 (2018).
24. Liu, Q. et al. The role of drop shape in impact and splash. *Nat. Commun.* **12**, 3068 (2021).
25. Vu, D. L., Le, C. D., Vo, C. P. & Ahn, K. K. Surface polarity tuning through epitaxial growth on polyvinylidene fluoride membranes for enhanced performance of liquid-solid triboelectric nanogenerator. *Compos. Part B Eng.* **223**, 109135 (2021).
26. Chen, Y. et al. Interfacial laser-induced graphene enabling high-performance liquid-solid triboelectric nanogenerator. *Adv. Mater.* **33**, 2104290 (2021).
27. Le, C.-D., Vo, C.-P., Nguyen, T.-H., Vu, D.-L. & Ahn, K. K. Liquid-solid contact electrification based on discontinuous-conduction triboelectric nanogenerator induced by radially symmetrical structure. *Nano Energy* **80**, 105571 (2021).
28. Shen, F. et al. Influence of temperature difference on performance of solid-liquid triboelectric nanogenerators. *Nano Energy* **99**, 107431 (2022).
29. Sun, W. et al. Liquid-solid triboelectric nanogenerators array and its applications for wave energy harvesting and self-powered cathodic protection. *Energy* **217**, 119388 (2021).
30. Hu, S. et al. Superhydrophobic liquid–solid contact triboelectric nanogenerator as a droplet sensor for biomedical applications. *ACS Appl. Mater. Inter.* **12**, 40021–40030 (2020).
31. Zhong, W. et al. Dripping channel based liquid triboelectric nanogenerators for energy harvesting and sensing. *ACS Nano* **14**, 10510–10517 (2020).
32. Jang, S. et al. Monocharged electret based liquid-solid interacting triboelectric nanogenerator for its boosted electrical output performance. *Nano Energy* **70**, 104541 (2020).
33. Choi, D. et al. Spontaneous occurrence of liquid-solid contact electrification in nature: Toward a robust triboelectric nanogenerator inspired by the natural lotus leaf. *Nano Energy* **36**, 250–259 (2017).
34. Zeng, Y., Luo, Y., Lu, Y. & Cao, X. Self-powered rain droplet sensor based on a liquid-solid triboelectric nanogenerator. *Nano Energy* **98**, 107316 (2022).
35. Zhang, P. et al. Biomimetic superhydrophobic triboelectric surface prepared by interfacial self-assembly for water harvesting. *Adv. Funct. Mater.* **35**, 2413201 (2025).
36. Tian, Z. et al. A sustainable NH₄⁺ ion battery by electrolyte engineering. *Adv. Funct. Mater.* **61**, e202213757 (2022).
37. Zhang, X. et al. Hydrogen bond-assisted ultra-stable and fast aqueous NH₄⁺ storage. *Nano-Micro Lett.* **13**, 139 (2021).
38. Cai, C. et al. Lightweight and mechanically robust cellulosic triboelectric materials for wearable self-powered rehabilitation training. *ACS Nano* **19**, 396–405 (2025).
39. Renard, J. J., Calidonna, S. E. & Henley, M. V. Fate of ammonia in the atmosphere—a review for applicability to hazardous releases. *J. Hazard. Mater.* **108**, 29–60 (2004).
40. Lin, S., Chen, X. & Wang, Z. L. Contact electrification at the liquid-solid interface. *Chem. Rev.* **122**, 5209–5232 (2022).
41. Luo, B. et al. Triboelectric probes for investigating charge transfer at the colloid-solid interface. *Nano Energy* **117**, 108874 (2023).
42. Krupa, S. V. Effects of atmospheric ammonia (NH₃) on terrestrial vegetation: a review. *Environ. Pollut.* **124**, 179–221 (2003).
43. Liu, Y. et al. Triboelectric tactile sensor for pressure and temperature sensing in high-temperature applications. *Nat. Commun.* **16**, 383 (2025).

Acknowledgements

This work was supported by Guangxi Natural Science Foundation of China (2023GXNSFFA026009, GKAD25069076) and the Innovation Project of Guangxi Graduate Education (YCBZ2024056).

Author contributions

T.L. and S.N. conceived the idea and designed the study. S.W. provided scientific guidance throughout. T.L. and X.L. designed experimental facility, Z.Y., H.H., X.C., S.Z., and C.C. observed the droplet morphology. K.Y., B.L., J.W., Y.L., and M.C. performed the electrical measurement and analyzed the data. T.L. and S.N. wrote the paper. All authors discussed the results and commented on the manuscript.

Competing interests

The authors declare no competing interests.

Additional information

Supplementary information The online version contains supplementary material available at <https://doi.org/10.1038/s41467-026-68974-4>.

Correspondence and requests for materials should be addressed to Shuangxi Nie.

Peer review information *Nature Communications* thanks Xia Liu, Zong-Hong Lin, and the other anonymous, reviewer(s) for their contribution to the peer review of this work. A peer review file is available.

Reprints and permissions information is available at <http://www.nature.com/reprints>

Publisher's note Springer Nature remains neutral with regard to jurisdictional claims in published maps and institutional affiliations.

Open Access This article is licensed under a Creative Commons Attribution-NonCommercial-NoDerivatives 4.0 International License, which permits any non-commercial use, sharing, distribution and reproduction in any medium or format, as long as you give appropriate credit to the original author(s) and the source, provide a link to the Creative Commons licence, and indicate if you modified the licensed material. You do not have permission under this licence to share adapted material derived from this article or parts of it. The images or other third party material in this article are included in the article's Creative Commons licence, unless indicated otherwise in a credit line to the material. If material is not included in the article's Creative Commons licence and your intended use is not permitted by statutory regulation or exceeds the permitted use, you will need to obtain permission directly from the copyright holder. To view a copy of this licence, visit <http://creativecommons.org/licenses/by-nc-nd/4.0/>.

© The Author(s) 2026